



OPEN

# Slab-derived devolatilization fluids oxidized by subducted metasedimentary rocks

Jay J. Ague<sup>1,2</sup>✉, Santiago Tassara<sup>1</sup>, Megan E. Holycross<sup>3</sup>, Ji-Lei Li<sup>4,5</sup>, Elizabeth Cottrell<sup>6</sup>, Esther M. Schwarzenbach<sup>7</sup>, Charalampos Fassoulas<sup>8</sup> and Timm John<sup>7</sup>

**Metamorphic devolatilization of subducted slabs generates aqueous fluids that ascend into the mantle wedge, driving the partial melting that produces arc magmas. These magmas have oxygen fugacities some 10–1,000 times higher than magmas generated at mid-ocean ridges. Whether this oxidized magmatic character is imparted by slab fluids or is acquired during ascent and interaction with the surrounding mantle or crust is debated. Here we study the petrology of metasedimentary rocks from two Tertiary Aegean subduction complexes in combination with reactive transport modelling to investigate the oxidative potential of the sedimentary rocks that cover slabs. We find that the metasedimentary rocks preserve evidence for fluid-mediated redox reactions and could be highly oxidized. Furthermore, the modelling demonstrates that layers of these oxidized rocks less than about 200 m thick have the capacity to oxidize the ascending slab dehydration flux via redox reactions that remove H<sub>2</sub>, CH<sub>4</sub> and/or H<sub>2</sub>S from the fluids. These fluids can then oxidize the overlying mantle wedge at rates comparable to arc magma generation rates, primarily via reactions involving sulfur species. Oxidized metasedimentary rocks need not generate large amounts of fluid themselves but could instead oxidize slab dehydration fluids ascending through them. Proposed Phanerozoic increases in arc magma oxygen fugacity may reflect the recycling of oxidative weathering products following Neoproterozoic–Palaeozoic marine and atmospheric oxygenation.**

Magmatic arcs above subduction zones produce most of the world's explosive volcanism and host giant ore deposits of copper, molybdenum, gold and other valuable metals. Arc magmas are considerably more oxidized than mid-ocean ridge basalts<sup>1–3</sup> and generate volcanic eruptions that can inject sulfur gases (mainly SO<sub>2</sub>) into the stratosphere, producing sulfate aerosols that trigger transient tropospheric cooling and stratospheric heating<sup>6</sup>. The origins of the oxidized signature in arcs, as well as in the underlying lithospheric mantle<sup>1–5,7</sup>, are vigorously debated<sup>4,8–23</sup>. One family of hypotheses holds that the fluids released by subducting slabs are inherently oxidized relative to the pristine igneous rocks generated at mid-ocean ridges. The oxidation may take place during seafloor hydrothermal alteration of mafic crust and/or serpentinization of ultramafic rocks at mid-ocean ridges before subduction. During subduction zone devolatilization, these rocks release fluids with a high oxidation potential to the mantle wedge and give rise to oxidized arc magmas via flux melting<sup>4,8–15</sup>. In contrast, another set of hypotheses posits that the oxidized signature is acquired in the mantle or crust overlying the subduction zone<sup>16,17</sup>. Some proposed oxidative pathways include the loss of reducing components (for example, H<sub>2</sub>) from ascending melts (or fluids) to the surrounding mantle<sup>16,18</sup> or fractional crystallization of Fe<sup>2+</sup>-rich phases such as garnet in deep lithospheric magma chambers<sup>19</sup>.

A corner-stone of this debate is determining whether subducting slabs can release oxidizing fluids. This has proved to be challenging, however, in part because many subducted lithologies lack mineral assemblages suitable for estimating oxygen fugacity ( $f_{O_2}$ ). Moreover, field-based studies and theoretical modelling have produced strongly conflicting results for the oxidation state of mafic

crust, underlying serpentinite and their respective fluids<sup>9–14,20–23</sup>. For example, some exhumed slab rocks preserve evidence for relatively reducing geochemical fingerprints<sup>20,21,23</sup>, whereas oxidizing fingerprints are preserved in others<sup>9,11,12,23</sup>.

The veneer (~400 m thick<sup>24</sup>) of sediments that covers subducted slabs worldwide provides another potential oxidative pathway but has received much less attention than other slab lithologies. Oxidized Fe<sup>3+</sup>-bearing sedimentary detritus containing goethite (FeO(OH)) and haematite (Fe<sub>2</sub>O<sub>3</sub>) from weathered continental sources can be transported to marine depositional settings thousands of kilometres from the shore (for example, the Bengal Fan<sup>25</sup>). Aeolian fluxes of oxidized minerals to deep ocean basins can occur on similar scales (for example, Indian and Pacific Oceans<sup>26</sup>). Furthermore, highly oxidized oceanic (meta)sediments (such as Fe- and Mn-rich cherts) are widely known from exhumed subduction complexes including those of California<sup>27</sup>, Japan<sup>27</sup> and New Zealand<sup>28</sup> in the Circum-Pacific region, the Alps<sup>29</sup> and other localities globally<sup>30</sup>. Moreover, the substantial oxidation potential of sediment entering subduction zones, such as the Mariana subduction zone, has been clearly documented in extensive ocean floor drill cores<sup>8,31</sup>. What is urgently needed now is a field-based evaluation of the redox states of subducted metasedimentary rocks and the extent to which they can regulate the  $f_{O_2}$  of devolatilization fluids released from downgoing slabs.

To address this important gap in knowledge, we investigated metasedimentary rocks from two forearc subduction complexes in the Aegean region, Greece (Methods and Extended Data Fig. 1). The samples are from three islands (Andros, Naxos and Tinos) that form part of the Cycladic Blueschist Unit (CBU) and from Crete.

<sup>1</sup>Department of Earth and Planetary Sciences, Yale University, New Haven, CT, USA. <sup>2</sup>Yale Peabody Museum of Natural History, New Haven, CT, USA.

<sup>3</sup>Department of Earth and Atmospheric Sciences, Cornell University, Ithaca, NY, USA. <sup>4</sup>Key Laboratory of Mineral Resources, Institute of Geology and Geophysics, Chinese Academy of Sciences, Beijing, China. <sup>5</sup>Innovation Academy for Earth Science, Chinese Academy of Sciences, Beijing, China. <sup>6</sup>Department of Mineral Sciences, National Museum of Natural History, Smithsonian Institution, Washington DC, USA. <sup>7</sup>Institut für Geologische Wissenschaften, Freie Universität Berlin, Berlin, Germany. <sup>8</sup>Natural History Museum of Crete, University of Crete, Heraklion, Greece. ✉e-mail: [jay.ague@yale.edu](mailto:jay.ague@yale.edu)

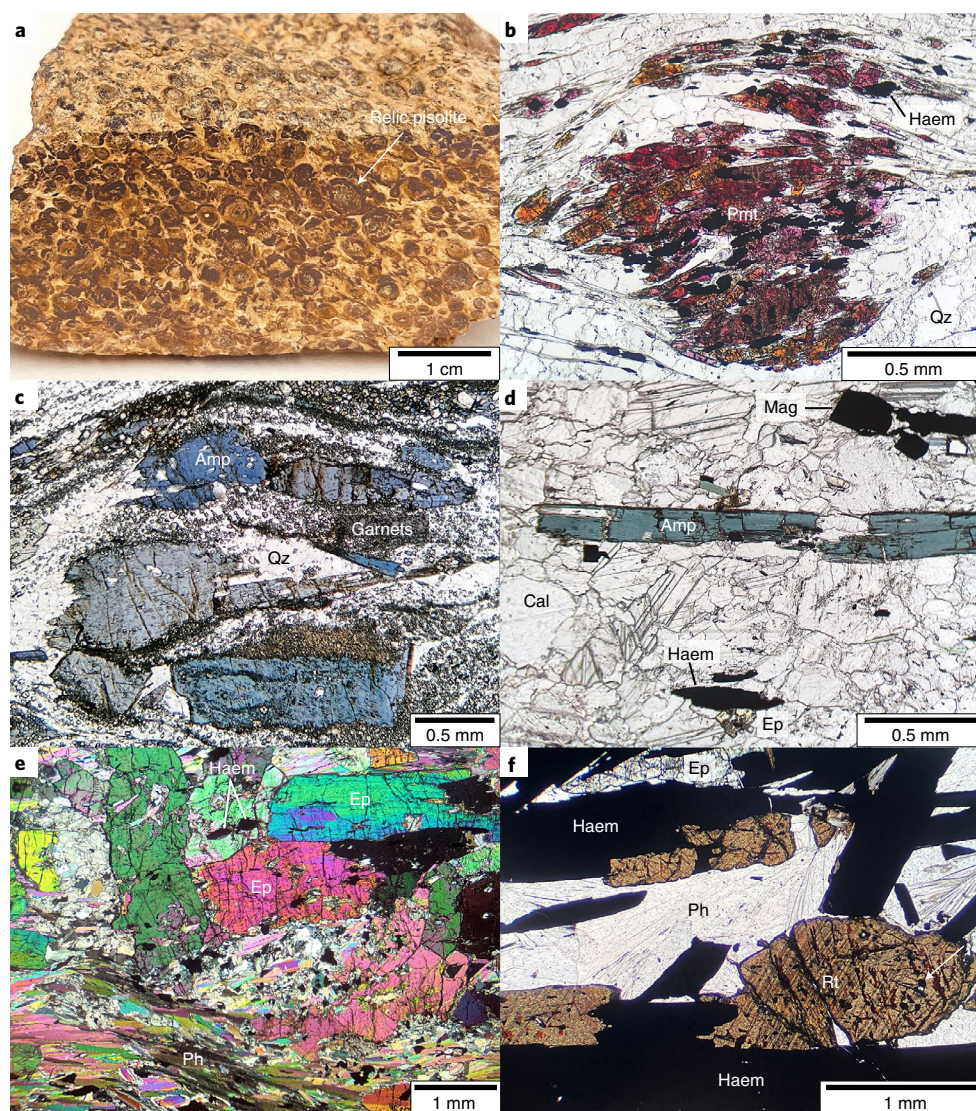


**Fig. 1 | Examples of highly oxidized metasedimentary rocks. a**, A hand sample of metabauxite from Crete (jagcr10A). Note the deformed elliptical relic soil pisolites (an example is marked by the white arrow). **b–f**, Photomicrographs taken under plane-polarized light unless otherwise noted. **b**, Aggregate of piemontite (Pmt) and haematite (Haem) in manganiferous quartzitic schist from Andros (jagan01A). Note the strong orange–pinkish red pleochroism in the piemontite. Qz, quartz. **c**, Sodium amphibole-bearing quartzite from Tinos. Note the abundant small Mn-rich garnets (jagti90B). Amp, amphibole. **d**, Glaucophane–ferro–glaucophane–riebeckite Na amphibole (blue) in marble with magnetite (Mag) and haematite from Tinos (jagti68B). Amphibole  $\text{Fe}^{3+}/(\text{Fe}^{2+} + \text{Fe}^{3+}) \approx 0.53$ . Cal, calcite; Ep, epidote. **e**, Epidote- and phengite-rich schist from Tinos (jagti108D; crossed polarizers). Ph, phengite. **f**, Coarse haematite and rutile (Rt) in vein from Tinos (jagti123A). Note the haematite inclusions in the rutile (an example is marked by the white arrow).

Both complexes reflect Tertiary subduction of the African plate beneath Eurasia, which continues today in the Hellenic subduction zone. The subduction complexes of the Aegean are among the most extensively studied and best-exposed on Earth.

### Oxidized rock types and textures

The oxidized rock types we investigated are likely to be less familiar than the classic blueschists and eclogites of subduction complexes. Because of the high  $\text{Fe}^{3+}$  contents of the rocks,  $\text{Fe}^{2+}$ -rich minerals including almandine-rich garnet porphyroblasts are uncommon or absent. Consequently, many of the rocks have an unremarkable appearance in outcrop. For this reason, we posit that oxidized metasediments have largely escaped attention in petrological studies and, thus, are probably much more common than is recognized at present. Moreover, they are not restricted to the islands we study; for example, oxidized metasedimen-

tary (and metaigneous) rocks are known from the CBU on Evia<sup>32</sup> and Sifnos<sup>11,33,34</sup>.

A wide variety of oxidized rock types are exposed, including metabauxite, which is well known from Crete and Naxos (>90 localities on Naxos alone<sup>35</sup>). The metabauxite protoliths were deep lateritic weathering horizons developed on carbonate sequences. Haematite and rutile are widespread, and relic soil pisolites were preserved in places (Fig. 1a).

On Andros, Mn- and Fe-rich quartzites and schists are found within a volcano-sedimentary sequence that hosts synsedimentary Mn mineralization. Garnets are rich in the spessartine component ( $\text{Mn}_3\text{Al}_2\text{Si}_3\text{O}_{12}$ ) and epidote can contain considerable piemontite ( $\text{Ca}_2\text{Mn}^{3+}\text{Al}_2\text{Si}_3\text{O}_{12}(\text{OH})$ ) (Fig. 1b). Similar rocks are found on neighbouring islands; over a dozen localities are known from Andros, Evia and Tinos<sup>32</sup>. Seafloor metasediments that are less manganiferous and contain abundant haematite  $\pm$  magnetite are not



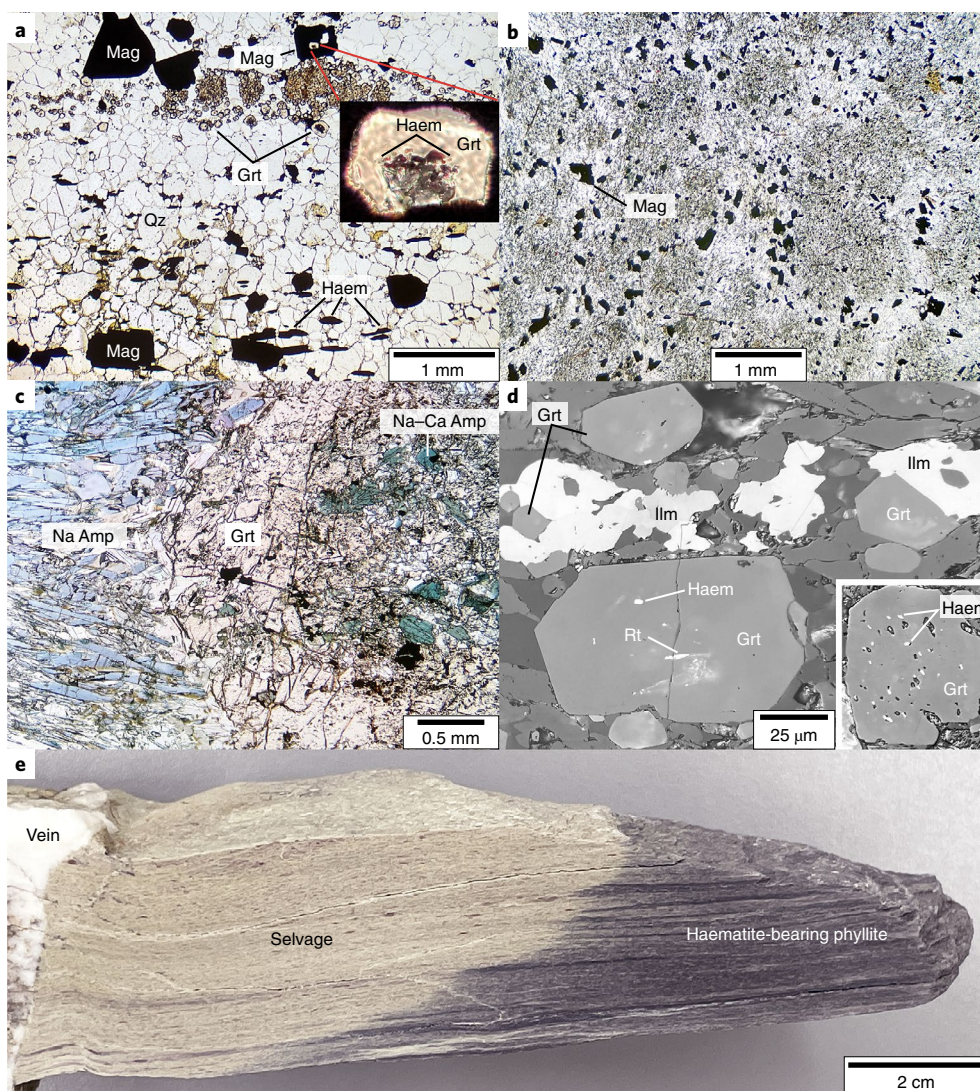


**Fig. 2 | Evidence for synmetamorphic reduction. a–c,** Plane-polarized light photomicrographs. **a,** Quartzite (jagti134N). Magnified inset shows haematite inclusions in a garnet (Grt) that is enclosed by magnetite. The rock initially contained only haematite, which was incorporated into growing garnets, but no magnetite. Subsequently, magnetite grew in the matrix and around garnets as a result of haematite reduction. Some haematite remains in the matrix. Garnet cores with haematite inclusions have high  $\text{Fe}^{3+}/(\text{Fe}^{3+} + \text{Fe}^{2+})$  values of ~0.35, whereas the rims have much lower values (~0.05). **b,** Albitite (jagti75A). Anastomosing ‘veinlets’ (light) containing magnetite formed by the reduction of fine-grained haematite are shown (haematite occurs in cloudy domains, which may also contain fine-grained albitite, quartz, phengite, epidote, sodic clinopyroxene, and Na and Na-Ca amphiboles (Amp)). These anastomosing features are interpreted as infiltration channels for reducing fluids. **c,** Garnet containing inclusions of Na-Ca amphibole (green, right) that have ~25% greater  $\text{Fe}^{3+}/(\text{Fe}^{3+} + \text{Fe}^{2+})$  values than matrix Na amphibole (blue, left) (jagti154F-1). The garnet core also contains small (tens of micrometres) inclusions of jadeite-aegirine clinopyroxene with ~0.4–0.6  $\text{Fe}^{3+}/(\text{Fe}^{3+} + \text{Al})$  (not visible). **d,** Reflected light photomicrograph showing haematite and rutile inclusions in garnet (main image and inset) and matrix ilmenite (Ilm) (jagti90B). Note that matrix ilmenite surrounds and postdates the haematite-bearing garnets. **e,** Cut rock slab containing the alteration selvage (tan ‘bleached’ appearance) adjacent to a quartz vein cutting purple-red haematite-bearing phyllite. The haematite has been destroyed in the selvage by reducing fluids that infiltrated along the vein (jagcr00A). Siderite-magnesite in veins is the inferred sink for the reduced iron.

uncommon; two quartzites from Tinos are studied herein (Figs. 1c and 2a,d). Their protoliths were probably cherts or sandstones.

Regionally widespread metapelitic phyllites and schists, as well as metacarbonate rocks, contain rhombohedral oxide  $\pm$  rutile  $\pm$  magnetite; we present examples from Tinos and Crete (Figs. 1d–f and 2c,e).

We also examined two rocks from Tinos that are intercalated with oxidized metasedimentary layers. One is an epidote- and Na amphibole-rich metabasaltic blueschist. The other is an Na-rich ‘albitite’ schist with complex mineralogy that includes Na amphibole, jadeite-aegirine (Na- $\text{Fe}^{3+}$ -Al) clinopyroxene, magnetite and

haematite (Fig. 2b). This highly sodic rock is reminiscent of jadeitite and may have similar origins<sup>36</sup>.

Multiple samples preserve textural evidence for reduction during metamorphism. For example, garnets whose cores contain only haematite inclusions can be found surrounded by matrix magnetite, indicating the reduction of haematite to magnetite some time after core growth (Fig. 2a). Garnet molar  $\text{Fe}^{3+}$  decreases ~70% from cores to rims (see Data availability). In another example, haematite-rich domains are cut by a network of Na amphibole-bearing veinlets in which haematite has been converted to coarse magnetite; these veinlets are inferred to be fluid infiltration pathways (Fig. 2b).

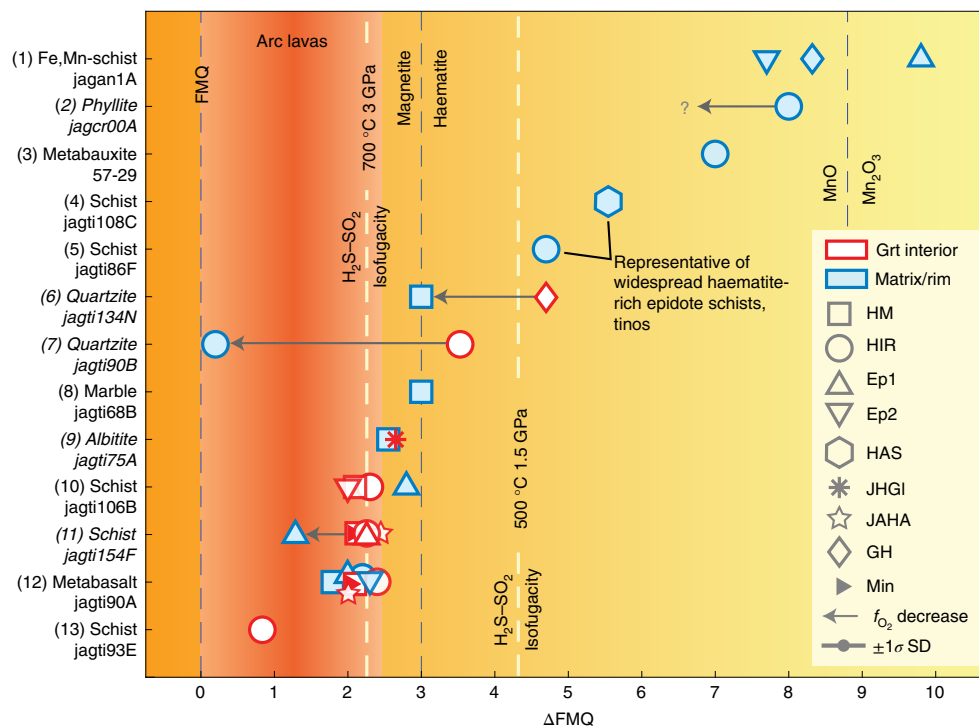


**Fig. 3 | Metamorphic  $f_{O_2}$ .** Values were calculated thermodynamically using coexisting mineral compositions measured with an electron probe microanalyser. HM, haematite-magnetite reaction; HIR, haematite-ilmenite-rutile reaction. The other reaction symbols are defined in the Methods. Red symbols are assemblages in garnet interiors and blue symbols are assemblages in matrix and/or garnet rims. The vertical red shaded band shows the approximate range of arc magma  $\Delta FMQ$  values<sup>4,5</sup>. The grey arrows denote  $f_{O_2}$  decrease during metamorphism. Italic sample types on the left denote those preserving evidence for synmetamorphic reduction (Fig. 2). Min denotes a minimum  $f_{O_2}$  estimate. Calculations were done at Cycladic pressure-temperature conditions of 500 °C and 1.5 GPa, except for sample (2), for which 400 °C and 1.0 GPa were used. The  $f_{O_2}$  corresponding to  $f_{H_2S} = f_{SO_2}$  isofugacity is shown for 500 °C and 1.5 GPa and for subarc conditions of 700 °C and 3.0 GPa. Orange-to-yellow background shading represents an increase in oxygen fugacity from left to right. The  $\pm 1\sigma$  standard deviation (SD) uncertainty on the oxygen fugacity estimates is shown in the legend. See Methods for calculation details and sample descriptions, and Supplementary Table 1 for  $\Delta FMQ$  values.

Figure 2c shows a garnet core that contains  $Fe^{3+}$ -rich Na-Ca amphibole and clinopyroxene, whereas the matrix contains glaucophane with  $Fe^{2+} > Fe^{3+}$ . In Fig. 2d, haematite is found in garnet interiors, but the matrix hosts  $Fe^{3+}$ -poor ilmenite. A redox profile is shown in phyllite from Crete, in which the rock distal to a cross-cutting quartz vein is rich in haematite, whereas the altered selvage rock proximal to the vein lacks haematite and is strongly depleted in iron (Fig. 2e).

### $f_{O_2}$ estimates

We used various combinations of eight independent oxybarometers to estimate metamorphic  $f_{O_2}$  (Methods), including the simple haematite-magnetite and haematite-ilmenite-rutile equilibria that are independent of the activity of  $H_2O$ . When possible, equilibria were applied to assemblages within garnet (preserved as inclusions) and in the rock matrix to evaluate  $f_{O_2}$  changes during metamorphism.

Figure 3 shows that metasedimentary lithologies can preserve a highly oxidized signature during subduction. The estimates of  $f_{O_2}$  relative to the fayalite-magnetite-quartz buffer (in  $\log_{10}$  units;  $\Delta FMQ$ ) cover an extraordinary range exceeding seven orders of magnitude; all are at or above the typical  $\Delta FMQ$  values of arc magmas. Rocks that lack magnetite can have  $f_{O_2}$  values that extend far above the haematite-magnetite buffer, up to  $\Delta FMQ \sim 9$ . These include Fe- and Mn-rich haematite-bearing schist, as well as haematite + rutile-bearing metabauxite, quartzite and metapelitic phyllite, and epidote-rich schist (samples 1–5). The extreme  $f_{O_2}$  of the manganese-rich metasediments is consistent with comparable localities elsewhere<sup>29</sup>. Another substantial fraction of the rock suite, which

includes marble, quartzite, metabasalt intercalated with oxidizing metasediments and metapelitic schist, clusters between  $\Delta FMQ \approx 2$  and the haematite-magnetite buffer (samples 6–12).

Inclusion assemblages within garnet may record  $f_{O_2}$  values that are  $\sim 1$ – $4 \log_{10}$  units higher than matrix assemblages. This is consistent with textural evidence and indicates synmetamorphic reduction following initial garnet growth (Fig. 2a,c,d), as has also been documented in metabasalts<sup>11</sup>. Furthermore, reduction need not cause a drop in  $f_{O_2}$ . For example, in Fig. 2b, the magnetite-rich veinlets formed at the expense of the intervening haematite-rich domains, but magnetite and haematite coexist. Thus, although the conversion of haematite to magnetite was proceeding, both phases were present so the  $f_{O_2}$  was constrained to be near the haematite-magnetite buffer as the bulk-rock  $Fe^{2+}/Fe^{3+}$  increased. We infer that reactive fluids ascending from deeper in the slab caused the reduction documented in Figs. 2 and 3 and were oxidized as a result.

### Fluid fluxes and metasedimentary rock oxidizing capacity

The time-integrated fluid flux ( $q_{TI}$ ;  $m^3_{fluid} m_{rock}^{-2}$ ) must be used to evaluate changes in redox state due to the infiltration of externally derived reactive fluids (Methods). Consider a rock column with  $1 m^2$  cross-sectional area extending vertically through a slab. Devolatilization fluids are progressively released and flow up and out of this column into the mantle wedge as the slab (and column) descends. Thus,  $q_{TI}$ , as measured at the top of the column, increases with depth. For the subarc depth interval 80–150 km, we took  $q_{TI} = 220 m^3_{fluid} m_{rock}^{-2}$  (refs. 21,24). The fluid flux generated by



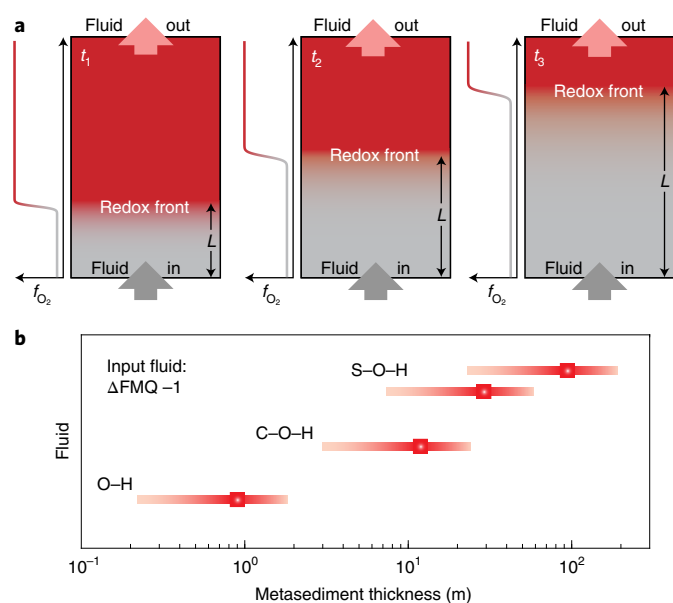
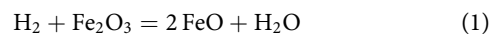


**Fig. 4 | Redox front propagation.** **a**, Model in which relatively low  $f_{O_2}$  ( $\Delta FMQ -1$ ) devolatilization fluids derived from deeper in the slab enter the base of an oxidizing metasedimentary rock sequence. The incoming fluids become oxidized as they reduce the rock. The time-integrated fluid flux increases with time. Consequently, as time progresses ( $t_1$ – $t_3$ , from left to right), the boundary (or redox front) between the reduced rock (shaded grey) and the remaining oxidized rock (shaded red) moves upwards. Oxidized fluids will continue to leave the top of the system unless the front propagation distance  $L$  reaches the available thickness of metasediment, at which point the buffer capacity of the metasedimentary sequence is exhausted. **b**, Thicknesses of oxidizing metasedimentary sequences required to oxidize the slab devolatilization flux of  $220 \text{ m}^3 \text{ m}^{-2}$  for model O–H, C–O–H and S–O–H fluids. For each fluid composition, the red bars denote the minimum and maximum thicknesses considered, corresponding to reduction of 20 wt% and 2.5 wt% rock  $\text{Fe}_2\text{O}_3$ , respectively, for input fluids at  $\Delta FMQ -1$ . Representative values for 5 wt% reduction are shown by the red squares. Two ranges for S–O–H fluids are shown; results for the molecular approach calculated herein give smaller values ( $\sim 5$ – $60 \text{ m}$ ) than the DEW approach<sup>21,41</sup> ( $\sim 20$ – $200 \text{ m}$ ).

local devolatilization of metasediment is over 1,500 times smaller and will therefore be dominated by the external flux ascending from deeper in the slab (Supplementary Information). Some reduction begins in the forearc (Figs. 2 and 3), but most is expected in the subarc where  $>80\%$  of the fluid release in the 0–150 km depth interval occurs<sup>21,24</sup>. In addition,  $\sim 40\%$  of the forearc fraction is derived from metasediments<sup>21,24</sup>, if they were inherently oxidized, they would release oxidized fluids during dehydration.

We used reaction-transport theory to assess whether oxidizing metasediments have the capacity to oxidize these fluids<sup>37–39</sup> (Methods). For one-dimensional reactive transport dominated by advection (flow), the reacted and unreacted rocks are separated by a reaction (redox) ‘front’ that propagates in the flow direction (Fig. 4a). The amount of bulk-rock  $\text{Fe}_2\text{O}_3$  reduced, the fluid composition and a redox reaction are required for the calculations (Fe is the most abundant redox-sensitive element). We investigated reductions of 2.5, 5, 10 and 20 wt% bulk-rock  $\text{Fe}_2\text{O}_3$ , the likely range for the studied lithologies (Methods), by O–H, C–O–H and S–O–H fluids at representative subarc conditions of  $700^\circ\text{C}$  and 3 GPa. We note that for a given fluid flux, reaction fronts for different chemical or isotopic tracers will travel different distances as a function of their partitioning behaviour<sup>37</sup>.

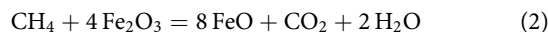
The reduction of one mole of  $\text{Fe}_2\text{O}_3$  by molecular  $\text{H}_2$  in aqueous (O–H) fluids can be described by



$\text{FeO}$  and  $\text{Fe}_2\text{O}_3$  are considered to be generically present in oxides or silicates. The fluid composition can be determined if  $f_{O_2}$  is known. Dehydration fluids released from relatively reducing subarc mafic crust and serpentinite are probably in the  $\Delta FMQ$  range 1 to  $-2$  (refs. 20,21,23); we took  $-1$  as representative. The  $\Delta FMQ$  of the haematite–magnetite buffer is representative of the oxidized metasediments and thus the fluids released from the top of the slab. With these bounding  $\Delta FMQ$  values, we could quantify the capacity of the metasediments to oxidize the dehydration fluids passing through the slab cover into the mantle wedge at subarc conditions. The calculations were not particularly sensitive to the metasedimentary  $f_{O_2}$  value as long as it was around or above that of haematite–magnetite. We note that some slabs may release more oxidized fluids<sup>9,13,23</sup>; these would be little modified by flow through the oxidized metasediments.

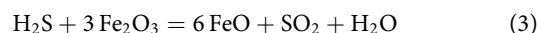
Figure 4b shows how thick metasedimentary layers would need to be to oxidize the slab dehydration flux. For O–H fluids, they are remarkably thin, ranging between  $\sim 20 \text{ cm}$  (20 wt%  $\text{Fe}_2\text{O}_3$  reduced) and  $\sim 2 \text{ m}$  (2.5 wt%  $\text{Fe}_2\text{O}_3$  reduced). This is because the amount of  $\text{H}_2$  in the ascending dehydration fluids is small, and the redox buffer capacity of the metasediments is large<sup>39,40</sup>.

In C–O–H fluids, one mole of methane ( $\text{CH}_4$ ) will reduce four moles of  $\text{Fe}_2\text{O}_3$



We calculated the input  $\text{CH}_4$  mole fraction ( $X_{\text{CH}_4}$ ) assuming graphite saturation, which yielded the maximum possible  $X_{\text{CH}_4}$  and is thus the most conservative value. Thicker sequences of metasediment are required to oxidize this flux relative to the O–H case (Fig. 4b). This is because the  $\text{CH}_4$  concentrations are higher than those of  $\text{H}_2$ , and the  $\text{CH}_4$ : $\text{Fe}_2\text{O}_3$  ratio is 1:4. Nonetheless, the thicknesses are still only  $\sim 10$ – $30 \text{ m}$ . As  $X_{\text{CH}_4}$  in the input fluid is still relatively small, the evolved  $\text{CO}_2$  is also small and will, in general, not precipitate carbonate phases unless they were already stable in the rock.

$\text{S}^{2-}$  species will be dominant in S–O–H fluids at low  $f_{O_2}$  (refs. 21,23). The oxidation of  $\text{H}_2\text{S}$  to produce  $\text{SO}_x$  can be represented using  $\text{SO}_2$  (ref. 23), the most abundant S species in volcanic gases<sup>6</sup>



Fluid and/or minerals can host the product Fe and S. For such reactions to go strongly to the right,  $f_{O_2}$  must be above that for  $f_{\text{H}_2\text{S}} = f_{\text{SO}_2}$  (isofugacity; Methods). As shown in Fig. 3, this would be the case for the highest  $f_{O_2}$  rocks at forearc conditions; the  $f_{O_2}$  for isofugacity drops sharply with increasing pressure ( $P$ ) and temperature ( $T$ ) and would be below haematite–magnetite at  $T > \sim 650^\circ\text{C}$  for typical subduction geotherms. Thus,  $\text{SO}_x$  will be important in fluids equilibrated with oxidized subarc metasediments.

For O–H and C–O–H fluids we used molecular  $\text{H}_2$ ,  $\text{CH}_4$  and  $\text{CO}_2$  as their thermodynamic and mixing properties are reasonably well established (Methods). For S–O–H fluids, calculations based on aqueous species<sup>21</sup> including  $\text{H}_2\text{S}_{\text{aq}}$  (the DEW model<sup>41</sup>) tend to give higher total S concentrations than those based on molecular  $\text{H}_2\text{S}$ . We calculated the input mole fraction  $X_{\text{H}_2\text{S}}$  at  $\Delta FMQ -1$  using the molecular approach for typical mid-ocean ridge basalt<sup>42</sup> at pyrite saturation to represent fluids exiting the top of the metaigneous portion of the slabs. The  $\text{H}_2\text{S}$ : $\text{Fe}_2\text{O}_3$  ratio will vary depending on the valence of S in  $\text{SO}_x$ ; the maximum ratio is 1:4 (for sulfate). Taking  $\text{H}_2\text{S}$ : $\text{Fe}_2\text{O}_3 = 0.25$ , the metasediment thickness needed to oxidize the

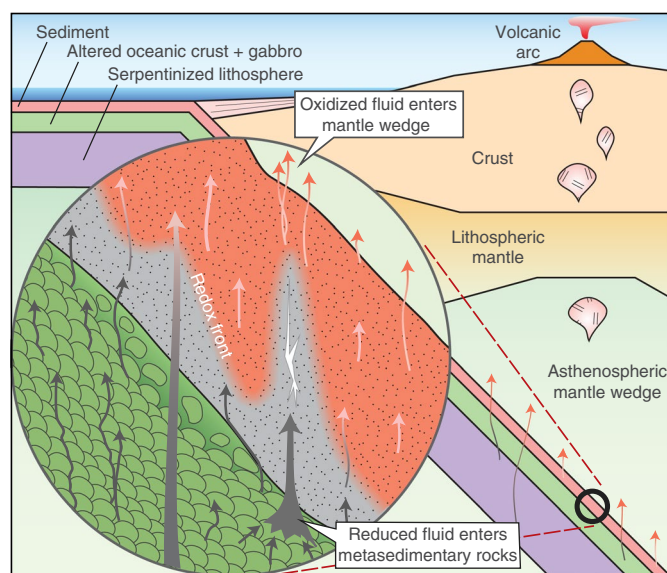


**Fig. 5 | Schematic illustration of the metasedimentary oxidative filter model.** Devolatilization fluids, derived from the dehydration of metagneous rocks, ascend from the slab and encounter oxidized metasedimentary rocks along the slab–mantle interface. The fluids reduce the oxidized rocks (grey) and become oxidized themselves (red). Oxidized fluids will flow upwards into the overlying mantle wedge provided the buffer capacity of the metasedimentary sequence is not exceeded. Channelways such as high-permeability conduits or veined areas (white) transmit a greater flux. If the metagneous devolatilization fluids were already oxidized, they would pass through the metasediments with their oxidizing character intact. In the inset diagram, an accumulation of pillow basalts is shown in green.

slab flux is greater than that for the O–H or C–O–H cases but is <60 m (Fig. 4b). Using S concentrations from aqueous species calculations<sup>21</sup> yielded greater thicknesses (<200 m).

Thicknesses for a C–S–O–H input devolatilization fluid at graphite and pyrite saturation are approximately the sum of the C–O–H and S–O–H results of Fig. 4b; this yielded a maximum of ~200 m. If O–H, C–O–H or S–O–H ± C input fluids had  $f_{O_2}$  values higher than  $\Delta FMQ - 1$ , all of the thicknesses in Fig. 4b would be decreased, as such fluids have less reducing power. For example, for a graphite-saturated C–O–H fluid at FMQ, the layer thicknesses decrease to <3 m.

Graphitic carbon is not common, occurring in isolated metasedimentary horizons intercalated with more oxidized rocks. The fluids in graphitic rocks need not be very reducing. Assuming the mean regional fluid  $X_{CO_2}$  for the CBU to be  $0.007 \pm 0.001$  ( $2\sigma$ )<sup>43</sup> together with the reaction  $C + O_2 = CO_2$  yielded  $\Delta FMQ \sim 0.3 \pm 0.1$  at graphite saturation. As most CBU rocks lack graphitic carbon, this is a minimum estimate. Regardless, as noted above, fluids near FMQ equilibrated with graphitic carbon would have little ability to reduce oxidized metasediments.

### The metasedimentary oxidative filter

Our results show that oxidized metasedimentary rocks have the capacity to oxidize the dehydration flux of fluids ascending from slabs at subarc depths. In general, metasedimentary rocks will be at the top of a slab and, thus, will be the last rock type encountered by the fluids before they enter the mantle wedge. Consequently, oxidized metasediments will act as an ‘oxidative filter’ that imposes a high- $f_{O_2}$  fingerprint on the slab fluids that ultimately drive flux melting and arc magmatism (Fig. 5). This model can reconcile evidence for the release of relatively reducing (for example,

H<sub>2</sub>S-bearing) fluids from subducted metabasalts and serpentinites in the subarc<sup>20,21,44,45</sup> with the presence of an oxidized (for example, sulfate-bearing) slab fluid component<sup>46</sup> in arc lavas<sup>10,14</sup>. In addition, any high- $f_{O_2}$  fluids generated in underlying hydrothermally altered metabasalt or serpentinite<sup>9,11,13</sup> would pass through the filter with their oxidizing character preserved. Moreover, the filter does not preclude oxidation processes operating in the overlying mantle wedge or lithosphere. Such metasediments could also undergo dehydration or partial melting<sup>45</sup> themselves, contributing to the oxidized flux.

The O–H and C–O–H fluid models require reduction of <10% of an average subducted sedimentary sequence (400 m thick<sup>24</sup>) to oxidize the slab flux. The S–O–H models require a higher, but still reasonable, proportion of <~15–50%. Consequently, the oxidizing potential of the metasedimentary sequence could be realized even if the rocks experienced thinning by offscraping in an accretionary prism or by compaction, if flow was channelized or if the sequence was not composed entirely of oxidized metasediments. On the other hand, thrust faulting or folding in the subduction channel would lead to greater thicknesses. A further implication is that considerable amounts of surface-derived oxenic components in slabs could be subducted past the subarc deep into the mantle, consistent with geochemical modelling<sup>47</sup> and an oxygen mass balance of the Marianas subduction zone<sup>8</sup>.

A rough assessment suggests that fluids ascending from metasediments could oxidize the mantle at a rate of  $\sim 4 \text{ km}^3 \text{ yr}^{-1}$ , comparable to the global arc magma generation rate of  $\sim 2.5 \text{ km}^3 \text{ yr}^{-1}$  (ref. 48; Supplementary Information). The majority of this oxidation would be accomplished by sulfur species, highlighting their much greater efficacy as redox agents relative to O–H and C–O–H species<sup>4,8,23,47</sup>. Nonetheless, O–H and C–O–H species could still contribute to the total.

The  $f_{O_2}$  of arc magmas ranges over two to three orders of magnitude<sup>2–5</sup>. At least some of this variability could be related to the oxidative capacity of subducted metasedimentary sequences. Some sequences of oceanic affinity, such as the Palaeozoic Tianshan high-pressure/ultrahigh-pressure metamorphic belt<sup>49</sup>, are relatively poor in oxenic components<sup>21</sup>. By contrast, oxidative weathering-derived detritus would be expected to be important in depositional basins more proximal to continents. The Aegean setting represents a hybrid case that contains both oxidized oceanic (for example, Mn-rich) and weathering-related sedimentary source components. Whether flow is pervasive or channelized to some degree<sup>12,21,50–52</sup> will increase the variability of the redox signal delivered to arcs. Postulated increases in the  $f_{O_2}$  of Phanerozoic island arcs relative to Precambrian equivalents<sup>53</sup> may be related to the global emergence of oxidative weathering driven by Neoproterozoic–Palaeozoic marine and atmospheric oxygenation<sup>54–56</sup>, and thus reflect the ultimate recycling of weathering products in subduction zones.

### Online content

Any methods, additional references, Nature Research reporting summaries, source data, extended data, supplementary information, acknowledgements, peer review information; details of author contributions and competing interests; and statements of data and code availability are available at <https://doi.org/10.1038/s41561-022-00904-7>.

Received: 17 August 2021; Accepted: 16 January 2022;  
Published online: 17 March 2022

### References

- Wood, B. J., Bryndzia, T. & Johnson, K. E. Mantle oxidation state and its relationship to tectonic environment and fluid speciation. *Science* **248**, 337–345 (1990).
- Carmichael, I. S. E. The redox states of basic and silicic magmas: a reflection of their source regions? *Contrib. Mineral. Petrol.* **106**, 129–141 (1991).

3. Frost, B. R. & Lindsley, D. H. Equilibria among Fe-Ti oxides, pyroxenes, olivine, and quartz: part II. Application. *Am. Mineral.* **77**, 1004–1020 (1992).
4. Kelley, K. A. & Cottrell, E. Water and the oxidation state of subduction zone magmas. *Science* **325**, 605–607 (2009).
5. Evans, K. A., Elburg, M. A. & Kamenetsky, V. S. Oxidation state of subarc mantle. *Geology* **40**, 783–786 (2012).
6. Robock, A. Volcanic eruptions and climate. *Rev. Geophys.* **38**, 191–213 (2000).
7. Birner, S. K. et al. Forearc peridotites from Tonga record heterogeneous oxidation of the mantle following subduction initiation. *J. Petrol.* **58**, 1755–1780 (2017).
8. Brounce, M., Cottrell, E. & Kelley, K. A. The redox budget of the Mariana subduction zone. *Earth Planet. Sci. Lett.* **528**, 115859 (2019).
9. Debret, B. & Sverjensky, D. A. Highly oxidising fluids generated during serpentinite breakdown in subduction zones. *Sci. Rep.* **7**, 10351 (2017).
10. Bénard, A. et al. Oxidising agents in sub-arc mantle melts link slab devolatilisation and arc magmas. *Nat. Commun.* **9**, 3500 (2018).
11. Gerrits, A. R. et al. Release of oxidizing fluids in subduction zones recorded by iron isotope zonation in garnet. *Nat. Geosci.* **12**, 1029–1033 (2019).
12. Chen, S. et al. Molybdenum systematics of subducted crust record reactive fluid flow from underlying slab serpentine dehydration. *Nat. Commun.* **10**, 4773 (2019).
13. Walters, J. B., Cruz-Urbe, A. & Marschall, H. R. Sulfur loss from subducted altered oceanic crust and implications for mantle oxidation. *Geochem. Perspect. Lett.* **13**, 36–41 (2020).
14. Muth, M. J. & Wallace, P. J. Slab-derived sulfate generates oxidized basaltic magmas in the southern Cascade arc (California, USA). *Geology* **49**, 1177–1181 (2021).
15. Brounce, M. et al. Covariation of slab tracers, volatiles, and oxidation during subduction initiation. *Geochem. Geophys. Geosyst.* **22**, e2021GC009823 (2021).
16. Brandon, A. D. & Draper, D. S. Constraints on the origin of the oxidation state of mantle overlying subduction zones: an example from Simcoe, Washington, USA. *Geochim. Cosmochim. Acta* **60**, 1739–1749 (1996).
17. Lee, C.-T. A., Leeman, W. P., Canil, D. & Li, Z.-X. A. Similar V/Sc systematics in MORB and arc basalts: implications for the oxygen fugacities of their mantle source regions. *J. Petrol.* **46**, 2313–2336 (2005).
18. Tollan, P. & Hermann, J. Arc magmas oxidized by water dissociation and hydrogen incorporation in orthopyroxene. *Nat. Geosci.* **12**, 667–661 (2019).
19. Tang, M., Erdman, M., Eldridge, G. & Lee, C.-T. A. The redox “filter” beneath magmatic orogens and the formation of continental crust. *Sci. Adv.* **4**, eaar4444 (2018).
20. Piccoli, F. et al. Subducting serpentinites release reduced, not oxidized, aqueous fluids. *Sci. Rep.* **9**, 19573 (2019).
21. Li, J.-L. et al. Uncovering and quantifying the subduction zone sulfur cycle from the slab perspective. *Nat. Commun.* **11**, 514 (2020).
22. Li, J.-L., Klemm, R., Huang, G.-F., Ague, J. J. & Gao, J. Unravelling slab  $\delta^{34}\text{S}$  compositions from in-situ sulphide  $\delta^{34}\text{S}$  studies of high-pressure metamorphic rocks. *Int. Geol. Rev.* **63**, 109–129 (2021).
23. Evans, K. A. & Frost, B. R. Deserpentinization in subduction zones as a source of oxidation in arcs: a reality check. *J. Petrol.* **62**, egab016 (2021).
24. van Keken, P. E., Hacker, B. R., Syracuse, E. M. & Abers, G. A. Subduction factory: 4. Depth-dependent flux of  $\text{H}_2\text{O}$  from subducting slabs worldwide. *J. Geophys. Res.* <https://doi.org/10.1029/2010JB007922> (2011).
25. Abrajewitch, A., Van der Voo, R. & Rea, D. K. Variations in relative abundances of goethite and hematite in Bengal Fan sediments: climatic vs. diagenetic signals. *Mar. Geol.* **267**, 191–206 (2009).
26. Zhang, Q. et al. Mechanism for enhanced eolian dust flux recorded in North Pacific Ocean sediments since 4.0 Ma: aridity or humidity at dust source areas in the Asian interior? *Geology* **48**, 77–81 (2020).
27. Yamamoto, K. Geochemical characteristics and depositional environments of cherts and associated rocks in the Franciscan and Shimanto terranes. *Sediment. Geol.* **52**, 65–108 (1987).
28. Coombs, D. S., Dowse, M., Grapes, R., Kawachi, Y. & Roser, B. Geochemistry and origin of piemontite-bearing and associated manganese-rich schists from Arrow Junction, western Otago, New Zealand. *Chem. Geol.* **48**, 57–79 (1985).
29. Tumiati, S., Godard, G., Martin, S., Malaspina, N. & Poli, S. Ultra-oxidized rocks in subduction mélanges? Decoupling between oxygen fugacity and oxygen availability in a Mn-rich metasomatic environment. *Lithos* **226**, 116–130 (2015).
30. Cannà, E. & Malaspina, N. From oceanic to continental subduction: implications for the geochemical and redox evolution of the supra-subduction mantle. *Geosphere* **14**, 2311–2336 (2018).
31. Alt, J. C. & Burdett, J. W. Sulfur in Pacific deep-sea sediments (Leg 129) and implications for cycling of sediment in subduction zone. *Proc. ODP Sci. Results* **129**, 283–294 (1992).
32. Reinecke, T. Phase relationships of sursassite and other Mn-silicates in highly oxidized low-grade, high-pressure metamorphic rocks from Evvia and Andros Islands, Greece. *Contrib. Mineral. Petrol.* **94**, 110–126 (1986).
33. Evans, B. J. Reactions among sodic, calcic, and ferromagnesian amphiboles, sodic pyroxene, and deerite in high-pressure metamorphosed ironstone, Siphnos, Greece. *Am. Mineral.* **71**, 1118–1125 (1986).
34. Groppo, C., Forster, M., Lister, G. & Compagnoni, R. Glaucophane schists and associated rocks from Sifnos (Cyclades, Greece): new constraints on the P-T evolution from oxidized systems. *Lithos* **109**, 254–273 (2009).
35. Feenstra, A. *Metamorphism of Bauxites on Naxos, Greece*. PhD thesis, Rijksuniversiteit Utrecht, Geologica Ultraiectina 39 (1985).
36. Johnson, C. A. & Harlow, G. E. Guatemala jadeitites and albitites were formed by deuterium-rich serpentinizing fluids deep within a subduction zone. *Geology* **27**, 629–632 (1999).
37. Bickle, M. J. Transport mechanisms by fluid-flow in metamorphic rocks: oxygen and strontium decoupling in the Trois Seigneurs Massif—a consequence of kinetic dispersion? *Am. J. Sci.* **292**, 289–316 (1992).
38. Skelton, A. D. L., Graham, C. M. & Bickle, M. J. Lithological and structural controls on regional 3-D fluid flow patterns during greenschist facies metamorphism of the Dalradian of the SW Scottish Highlands. *J. Petrol.* **36**, 563–586 (1995).
39. Ague, J. J. Simple models of coupled fluid infiltration and redox reactions in the crust. *Contrib. Mineral. Petrol.* **132**, 180–197 (1998).
40. Wood, B. J. & Walther, J. V. In *Fluid-Rock Interactions During Metamorphism* (eds Walther, J. V. & Wood, B. J.) 89–107 (Springer, 1986).
41. Sverjensky, D. A. Thermodynamic modelling of fluids from surficial to mantle conditions. *J. Geol. Soc.* **176**, 348–374 (2019).
42. Gale, A., Dalton, C. A., Langmuir, C. H., Su, Y. & Schilling, J.-G. The mean composition of ocean ridge basalts. *Geochem. Geophys. Geosyst.* **14**, 489–518 (2013).
43. Stewart, E. M. & Ague, J. J. Pervasive subduction zone devolatilization recycles  $\text{CO}_2$  into the forearc. *Nat. Commun.* **11**, 6220 (2020).
44. Tomkins, A. G. & Evans, K. A. Separate zones of sulfate and sulfide release from subducted mafic oceanic crust. *Earth Planet. Sci. Lett.* **428**, 73–83 (2015).
45. Canil, D. & Fellows, S. A. Sulphide-sulphate stability and melting in subducted sediment and its role in arc mantle redox and chalcophile cycling in space and time. *Earth Planet. Sci. Lett.* **470**, 73–86 (2017).
46. Schwarzenbach, E. S. et al. Sulphur and carbon cycling in the subduction zone mélange. *Sci. Rep.* **8**, 15517 (2018).
47. Evans, K. A. The redox budget of subduction zones. *Earth Sci. Rev.* **113**, 11–32 (2012).
48. DePaolo, D. J. The mean life of continents: estimates of continent recycling rates from Nd and Hf isotopic data and implications for mantle structure. *Geophys. Res. Lett.* **10**, 705–708 (1983).
49. Bayet, L., John, T., Agard, P., Gao, J. & Li, J.-L. Massive sediment accretion at ~80 km depth along the subduction interface: evidence from the southern Chinese Tianshan. *Geology* **46**, 495–498 (2018).
50. John, T. et al. Volcanic arcs fed by rapid pulsed fluid flow through subducting slabs. *Nat. Geosci.* **5**, 489–492 (2012).
51. Plümpner, O., John, T., Podladchikov, Y. Y., Vrijmoed, J. C. & Scambelluri, M. Fluid escape from subduction zones controlled by channel-forming reactive porosity. *Nat. Geosci.* **10**, 150–156 (2017).
52. Piccoli, F., Ague, J. J., Chu, X., Tian, M. & Vitale Brovarone, A. Field-based evidence for intra-slab high-permeability channel formation at eclogite-facies conditions during subduction. *Geochem. Geophys. Geosyst.* **22**, e2020GC009520 (2020).
53. Stolper, D. A. & Bucholz, C. E. Neoproterozoic to early Phanerozoic rise in island arc redox state due to deep ocean oxygenation and increased marine sulfate levels. *Proc. Natl Acad. Sci. USA* **116**, 8746–8755 (2019).
54. Och, L. M. & Shields-Zhou, G. A. The Neoproterozoic oxygenation event: environmental perturbations and biogeochemical cycling. *Earth Sci. Rev.* **110**, 26–57 (2012).
55. Lyons, T. W., Reinhard, C. T. & Planavsky, N. J. The rise of oxygen in Earth's early ocean and atmosphere. *Nature* **506**, 307–315 (2014).
56. Sperling, E. A. et al. A long-term record of early to mid-Paleozoic marine redox change. *Sci. Adv.* **7**, eabf4382 (2021).

**Publisher's note** Springer Nature remains neutral with regard to jurisdictional claims in published maps and institutional affiliations.



**Open Access** This article is licensed under a Creative Commons Attribution 4.0 International License, which permits use, sharing, adaptation, distribution and reproduction in any medium or format, as long as you give appropriate credit to the original author(s) and the source, provide a link to the Creative Commons license, and indicate if changes were made. The images or other third party material in this article are included in the article's Creative Commons license, unless indicated otherwise in a credit line to the material. If material is not included in the article's Creative Commons license and your intended use is not permitted by statutory regulation or exceeds the permitted use, you will need to obtain permission directly from the copyright holder. To view a copy of this license, visit <http://creativecommons.org/licenses/by/4.0/>.

© The Author(s) 2022



## Methods

Mineral abbreviations follow Whitney and Evans<sup>57</sup>, except Haem is used for haematite. Amphibole nomenclature follows Hawthorne et al.<sup>58</sup>.

**Metamorphism.** The CBU underwent high-pressure/low-temperature metamorphism during the Eocene. Metamorphic *P–T* conditions reached 500–550 °C and 1.5–2.0 GPa (refs. <sup>59–61</sup>). The samples from Crete are from the Phyllite–Quartzite unit and the Plattenkalk nappe, which comprise the high-pressure/low-temperature rocks collectively known as the lower nappes<sup>62</sup>. Metamorphism occurred in the late Miocene and reached ~400 °C and ~1.0 GPa (refs. <sup>63,64</sup>).

**Thermodynamic data.** The thermodynamic calculations were done using the database of Holland and Powell<sup>65</sup>, incorporating the standard-state properties of H<sub>2</sub>O, CO<sub>2</sub>, H<sub>2</sub>, CH<sub>4</sub>, CO, H<sub>2</sub>S and S<sub>2</sub>, together with the equations of state of ref. <sup>66</sup> for H<sub>2</sub>O and CO<sub>2</sub> and ref. <sup>67</sup> for all others. Nonideal mixing among these was treated using the molecular models of refs. <sup>68,69</sup>. Thermodynamic data for SO<sub>2</sub> were also included<sup>70</sup>; the critical pressure was adjusted slightly from 7.87 MPa to 9.87 MPa to better fit available volume relations at elevated *P–T* conditions<sup>71</sup> using the equation of state of ref. <sup>67</sup>. SO<sub>2</sub> was assumed to mix ideally; this assumption had no impact on the  $f_{\text{H}_2\text{S}} - f_{\text{SO}_2}$  isofugacity calculations. Equilibria involving the above C–O–H–S species were calculated using Theriak-Domino<sup>72</sup> version 11.03.2020 (Supplementary Table 2). The ‘fluid’ standard state was adopted, which specifies unit activity of the pure substance at the *P–T* conditions of interest. O<sub>2</sub> was not considered as a fluid constituent because its concentrations are so low that there is effectively no free O<sub>2</sub> in the fluid<sup>39</sup>.

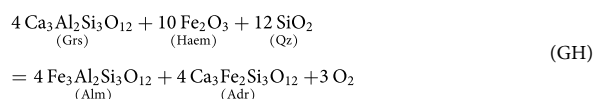
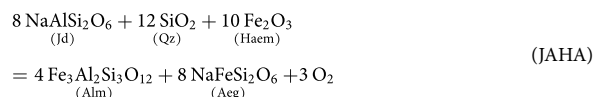
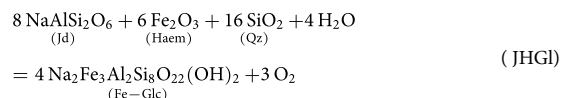
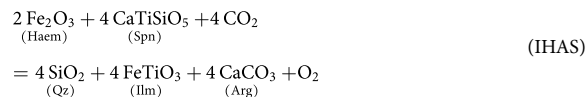
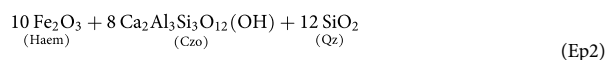
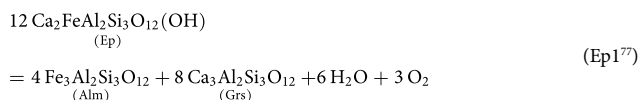
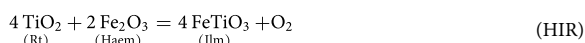
We estimated fluid S concentrations in two ways. First, we considered the average mid-ocean-ridge basalt composition of ref. <sup>42</sup> at ΔFMQ –1 with enough added S to stabilize pyrite at subarc conditions of 700 °C and 3 GPa (1.895 × 10<sup>–3</sup> molar S/Si ratio; Supplementary Information). Such fluids need not be generated in the metabasalt; they could also be derived from underlying reduced serpentinite that achieved redox equilibrium with metabasalt. Using the fluid standard-state model above and pseudosection calculations following ref. <sup>43</sup>, this yields a total S mole fraction of 5.6 × 10<sup>–4</sup> (almost entirely H<sub>2</sub>S).

Second, we considered the aqueous species treatment used in the DEW model<sup>41</sup> computed in ref. <sup>21</sup>. The standard state is: unit activity for a hypothetical 1 molal solution referenced to infinite dilution at the *P–T* conditions of interest. This treatment gives an average S mole fraction of 1.6 × 10<sup>–3</sup> for fluids released from metaigneous rocks when integrated over subarc depths of 75–150 km (ref. <sup>21</sup>). The two approaches should give comparable results as the fluids are supercritical<sup>23</sup>, but the DEW result is larger by a factor of ~3. We attribute this to the fact that DEW considers a much wider range of aqueous species than the molecular model, including Cl complexes, thus facilitating a better and more complete accounting of all sulfur species in fluids. We emphasize that a factor of ~3 difference is still quite good agreement for calculations of this nature, and that our conclusions regarding oxidation by metasediments are unaffected by the choice of model. Figure 4b shows the results of both approaches.

For the  $f_{\text{O}_2}$  estimates, nonideal mixing was considered for garnet<sup>73,74</sup>, epidote<sup>65</sup>, clinopyroxene<sup>75</sup>, haematite–ilmenite and amphibole; for the last two of these we used the models in the AX 62 program (T.J.B. Holland, University of Cambridge). For haematite–ilmenite, we calculated the AX 62 model with Theriak-Domino<sup>72</sup> to properly account for solvus relationships. The piemontite component was appreciable only for the Mn-bearing epidote from Andros (sample jagan1A). For this sample we used the model from Holland and Powell<sup>65</sup> for epidote–clinozoisite and added the piemontite endmember via ideal mixing. Quartz, rutile, magnetite, sphene and H<sub>2</sub>O were assumed to have unit activity; typical H<sub>2</sub>O mole fractions of ~0.99 or greater are documented for the Cyclades<sup>43</sup>.

**$f_{\text{O}_2}$  calculations.** Mineral compositions (Data availability) for  $f_{\text{O}_2}$  estimation were obtained using the JEOL JXA-8530F field-emission gun electron-probe microanalyser (EPMA) at Yale University. Analyses used natural and synthetic standards, off-peak background corrections, a 15 kV accelerating voltage and a 10 nA beam current. The beam diameter ranged from focused to 5 μm, depending on the grain size and mineral type (5 μm was used for all hydrous phases). Rhombohedral oxides in three of the four lowest- $f_{\text{O}_2}$  samples (ΔFMQ ~2–3; jagti90A, jagti106B, jagti154F) contain exsolution lamellae that were reintegrated with the host grain using multiple (up to 12) EPMA analysis spots per sample<sup>76</sup>.

We utilized the following equilibria



The last of these was used to compute the  $f_{\text{O}_2}$  for H<sub>2</sub>S–SO<sub>2</sub> isofugacity ( $f_{\text{H}_2\text{S}} = f_{\text{SO}_2}$ ) assuming unit activity of H<sub>2</sub>O ( $a_{\text{H}_2\text{O}} = 1$ ). Decreasing  $a_{\text{H}_2\text{O}}$  decreases the  $f_{\text{O}_2}$  for H<sub>2</sub>S–SO<sub>2</sub> isofugacity, but low  $a_{\text{H}_2\text{O}}$  fluids are unlikely<sup>43</sup>. Donohue and Essene<sup>77</sup> defined equilibrium Ep1 and used it to estimate  $f_{\text{O}_2}$  for several rocks, including high-pressure calcisilicate from the Bergen Arcs, Norway. They obtained high ΔFMQ in the range of 3.5–4 for the calcisilicate. This rock is from a continental subduction zone and was subjected to Neoproterozoic granulite facies metamorphism and potential metasomatism before the Palaeozoic high-pressure event. Thus, it is from a very different setting than that studied herein.

The mineral Fe<sup>3+</sup> contents were calculated by stoichiometry from the EPMA analyses. Haematite–ilmenite: 2 cations per 3 oxygens. Magnetite: 3 cations per 4 oxygens. Epidote: Fe<sup>3+</sup> + Mn<sup>3+</sup> + Al + Cr + Ti = 3 per 12.5 oxygens. We assumed all Mn<sup>3+</sup> for manganese-bearing epidote in sample jagan1A from Andros, and Mn<sup>2+</sup> for epidote in the other samples. Garnet: two octahedral sites per 12 oxygens (Fe<sup>3+</sup> + Al<sup>vi</sup> + Cr + Ti = 2). Very low garnet Fe<sup>3+</sup>/(Fe<sup>2+</sup> + Fe<sup>3+</sup>) estimates were deemed unreliable. This is mainly a concern for reaction GH, above, which involves an andradite component. Furthermore, the activity–composition relations for Fe<sup>3+</sup>-bearing garnet at low Fe<sup>3+</sup>/(Fe<sup>2+</sup> + Fe<sup>3+</sup>) are probably subject to large uncertainties. Consequently, we only used GH when the estimated garnet Fe<sup>3+</sup>/(Fe<sup>2+</sup> + Fe<sup>3+</sup>) was >0.25. Clinopyroxene: 4 cations per 6 oxygens. The studied clinopyroxenes are predominantly jadeite–aegirine solid solutions with high Fe<sup>3+</sup> contents that can be reasonably estimated by stoichiometry. Following the AX 62 program, we adopted a minimum Fe<sup>2+</sup>/(Fe<sup>2+</sup> + Fe<sup>3+</sup>) value of 0.05 for clinopyroxene. Amphiboles: the average of the least upper bound and greatest lower bound on Fe<sup>3+</sup> content as determined from a range of normalizations<sup>78</sup>. For these amphiboles, the two normalizations that were averaged were (1) total cations – (Na + K + Ca) = 13 and (2) total cations – K = 15 (both per 23 oxygens). Other normalizations yielded spurious negative Fe<sup>3+</sup> contents.

Most  $f_{\text{O}_2}$  estimates were made for the Cycladic *P–T* conditions of 500 °C and 1.5 GPa. Using 550 °C and 2 GPa yielded very similar results. For the low-grade sample from Crete, we used 400 °C and 1.0 GPa. Because we report  $f_{\text{O}_2}$  estimates in terms of ΔFMQ, the results are not strongly dependent on the *P–T* conditions used in the calculations (see uncertainty analysis).

The various oxybarometers involve different calculation assumptions but yielded comparable results for a given sample (Fig. 3 and Supplementary Table 1). Large variations in the activity of H<sub>2</sub>O would be expected to produce large variations in  $f_{\text{O}_2}$  estimates for H<sub>2</sub>O-bearing and H<sub>2</sub>O-absent equilibria in a given sample, but this was not observed. Magnetite is nearly pure, so we take  $a_{\text{Mag}} = 1$ ; the activity would have been less than that if magnetite originally contained impurities such as Ti<sup>4+</sup> that were lost subsequent to high-pressure/low-temperature metamorphism. However, there is no evidence for any such losses and using  $a_{\text{Mag}} < 1$  simply increases the haematite–magnetite  $f_{\text{O}_2}$  estimates.

**Uncertainty analysis.** We evaluated the effect of *P–T* uncertainties on  $f_{\text{O}_2}$  estimates for individual reactions using a Monte Carlo analysis of the haematite–magnetite buffer with 2σ uncertainties of ±50 °C and ±0.4 GPa. This yielded a standard deviation on ΔFMQ of ±0.22, which is comparable to that of Gerrits et al.<sup>11</sup> (±0.2) for the *P–T* effects on similar  $f_{\text{O}_2}$  calculations. The uncertainty is dependent on the reaction to some degree; a Monte Carlo analysis of the HIR buffer yielded a



smaller  $\Delta\text{FMQ}$  uncertainty of  $\pm 0.12$ . To evaluate the effects of uncertainties on mineral analyses, thermodynamic data and the extent and timing of equilibration, we calculated the standard deviation on  $\Delta\text{FMQ}$  with respect to the mean for four samples with multiple  $f_{\text{O}_2}$  estimates made using different reactions (jagti75A, jagti90A, jagti106B and jagti154F; 17 total estimates). This yielded a standard deviation of  $\pm 0.21$ . Summing this and the haematite–magnetite uncertainty in quadrature ( $\sqrt{0.22^2 + 0.21^2}$ ) yielded  $\pm 0.30$ , our preferred value for the standard deviation of an individual  $\Delta\text{FMQ}$  estimate. This is far smaller than the observed range of  $\sim 9 \log_{10}$  units (Fig. 3). The uncertainties for the Mn-rich sample from Andros (jagan1A-1) are deemed larger due to uncertainties in the thermodynamic properties of clinozoisite–epidote–piromontite solid solutions. Nonetheless, the extremely high  $f_{\text{O}_2}$  of such rocks is clear ( $\Delta\text{FMQ} \sim 9$ ) and is comparable to estimates made on similar rocks elsewhere<sup>29</sup>.

**Time-integrated fluid flux calculations and the fluid:rock ratio.** The fluid:rock ratio (FRR) is a measure of the amount of fluid infiltration needed to drive a given reaction in a rock, but in general it will underestimate the fluid flux required to propagate a reaction front. Consider a volumetric FRR of  $1 \text{ m}^3_{\text{fluid}} \text{ m}^{-3}_{\text{rock}}$ . This seems like a modest number, but it only considers a rock volume in isolation and does not account for the spatial extent of flow. Imagine a 1-km-long vertical column of rock with a  $1 \text{ m}^2$  cross-section through which this fluid flows vertically. To react the entire column,  $1 \text{ m}^3$  of fluid is required for every  $1 \text{ m}^3$  of rock (the FRR). Thus,  $1,000 \text{ m}^3$  of fluid is required to react  $1,000 \text{ m}^3$  of rock, far greater than the FRR implies. The FRR must be multiplied by the length scale of flow to obtain the time-integrated fluid flux<sup>37</sup> ( $q_{\text{TI}}$ ), yielding  $1,000 \text{ m}^3_{\text{fluid}} \text{ m}^{-2}_{\text{rock}}$  for our example.

The one-dimensional conservation of mass expression describing fluid advection (flow) with chemical reaction for a chemical species,  $s$ , in the fluid is<sup>79</sup>

$$\frac{\partial(\phi C_s)}{\partial t} = -\frac{\partial(\bar{v}_x \phi C_s)}{\partial x} + \phi \sum_l R_{s,l} \quad (4)$$

in which  $C_s$  is the concentration of  $s$  ( $\text{mol m}^{-3}_{\text{fluid}}$ ),  $\bar{v}_x$  is the average flow velocity in the  $x$  direction ( $\text{m s}^{-1}$ ),  $\phi$  is the porosity,  $R_{s,l}$  is the rate of production or consumption of  $s$  by reaction  $l$  ( $\text{mol m}^{-3}_{\text{fluid}} \text{ s}^{-1}$ ) and  $t$  is time. Assuming local fluid–rock chemical equilibrium, one simple overall redox reaction ( $l = 1$ ) and constant porosity, this expression can be integrated and recast to give  $q_{\text{TI}}$  at the fluid inlet<sup>39</sup>

$$q_{\text{TI}} = \left( \frac{M_s V_f}{\Delta X_s} \right) L + L \phi \quad (5)$$

Here,  $L$  is the length of a unit column of rock that has been reacted. A reaction front, which moves in the direction of flow, separates the reacted and unreacted regions (Fig. 4a). The  $V_f$  term is the molar volume of the fluid,  $M_s$  is the moles of  $s$  produced or consumed per unit volume rock and  $\Delta X_s$  is the difference between the mole fraction of  $s$  in the fluid upstream and downstream of the front. The term in parentheses on the right-hand side of the equation is the volumetric FRR ( $\text{m}^3_{\text{fluid}} \text{ m}^{-3}_{\text{rock}}$ ). The  $L\phi$  term is negligible if the porosity is small<sup>37–39</sup>; we set  $\phi = 0.001$  (ref. <sup>80</sup>). Even the comparatively large value of  $\phi = 0.01$  contributes only  $1 \text{ m}^3 \text{ m}^{-2}$  to  $q_{\text{TI}}$  for  $L = 100 \text{ m}$  front propagation. We take  $V_f = 1.495 \times 10^{-5} \text{ m}^3 \text{ mol}^{-1}$ , the value for  $\text{H}_2\text{O}$  at  $700^\circ\text{C}$  and  $3.0 \text{ GPa}$  (ref. <sup>66</sup>).

If the metasedimentary sequence is too thin then the buffer capacity of the rocks will be exceeded; some of the incoming fluid will be oxidized, but not all of it. Thus, to be conservative and constrain the maximum thicknesses required, we modelled the largest likely redox state changes. These involved the most reduced reactant valences and the most oxidized product valences:  $\text{H}_2$ – $\text{H}^+$ ,  $\text{C}^{4-}$ – $\text{C}^{4+}$  and  $\text{S}^{2-}$ – $\text{S}^{6+}$ . Although there may be variations in speciation on the product side of the overall reactions, our main concern was the nature and concentration of the reducing species that enter the rock. For the O–H, C–O–H and S–O–H fluids we considered, these species were dominantly  $\text{H}_2$ ,  $\text{CH}_4$  and  $\text{H}_2\text{S}$ , respectively<sup>21,23,39,40</sup>. Aqueous  $\text{Fe}^{2+}$  and  $\text{Fe}^{3+}$  species were not considered as they are likely to be less important for long-distance redox transport<sup>23</sup>.

The molecular fluid compositions were calculated for representative subarc conditions of  $700^\circ\text{C}$  and  $3.0 \text{ GPa}$  (Supplementary Table 2). As discussed in the main text, input fluids were speciated at  $\Delta\text{FMQ} -1$ , and output fluids at the haematite–magnetite buffer ( $\Delta\text{FMQ} 2.5$ ). For example, for the O–H fluid, the input has a mole fraction  $\text{H}_2$  ( $X_{\text{H}_2}$ ) of  $6.20 \times 10^{-5}$ , whereas the output has  $1.06 \times 10^{-6}$  ( $>98\%$  of the  $\text{H}_2$  is oxidized). This yields a  $\Delta X_{\text{H}_2}$  value of  $6.094 \times 10^{-5}$ , which is very close to the input value because the output fluid has little  $\text{H}_2$ . For the C–O–H fluid,  $\Delta X_{\text{CH}_4}$  is  $1.85 \times 10^{-5}$ , and virtually all of the input  $\text{CH}_4$  is oxidized to produce  $\text{CO}_2$ . At  $700^\circ\text{C}$  and  $3.0 \text{ GPa}$ , haematite–magnetite is at a higher  $f_{\text{O}_2}$  than  $f_{\text{H}_2\text{S}} - f_{\text{SO}_2}$  isofugacity and, thus,  $\text{SO}_2$  will be in greater abundance than  $\text{H}_2\text{S}$  in the output fluid (Fig. 3). For the fluid standard-state S–O–H fluid, the  $X_{\text{H}_2\text{S}}$  in the input fluid is  $\sim 7$  times greater than the output, yielding  $\Delta X_{\text{H}_2\text{S}} = 4.78 \times 10^{-4}$ . This means that  $\sim 85\%$  of the input  $\text{H}_2\text{S}$  is oxidized (to produce  $\text{SO}_2$  and  $\text{S}_2$  in our calculation) at the haematite–magnetite buffer. The proportion is  $>95\%$  at  $\Delta\text{FMQ} 3.0$ . Minor  $\text{H}_2$  is also present in C–O–H and S–O–H fluids; its oxidation is treated as described above.

The  $M_s$  value is the amount of rock-hosted  $\text{Fe}^{3+}$  that can be reduced. Sample jagti68B had the lowest iron content in the sample suite ( $2.9 \text{ wt}\%$  as  $\text{Fe}_2\text{O}_3$ , total<sup>43</sup>). On average, the metabasites of Naxos contain  $\sim 20 \text{ wt}\%$  (ref. <sup>35</sup>). Consequently, we took the generous range of  $2.5$ – $20 \text{ wt}\%$  to represent the amount of  $\text{Fe}_2\text{O}_3$  available

for reduction. The total iron content could be higher; this range simply represents the mass fraction that is reduced. For a representative rock density of  $3,200 \text{ kg m}^{-3}$ ,  $1 \text{ wt}\%$   $\text{Fe}_2\text{O}_3$  corresponds to  $2.004 \times 10^2 \text{ moles Fe}_2\text{O}_3 \text{ m}^{-3}_{\text{rock}}$ . Reaction (1) shows that 1 mole of  $\text{H}_2$  will reduce 1 mole of  $\text{Fe}_2\text{O}_3$ . As a result, the  $M_{\text{H}_2}$  required to reduce  $1 \text{ wt}\%$  of  $\text{Fe}_2\text{O}_3$  is  $2.004 \times 10^2 \text{ moles H}_2 \text{ m}^{-3}_{\text{rock}}$ . The  $M_{\text{H}_2}$  values for other weight per cent values will scale proportionately. As noted in the text, the  $M_{\text{CH}_4}$  and  $M_{\text{H}_2\text{S}}$  values are  $0.25 M_{\text{H}_2}$  (for example, a  $\text{CH}_4/\text{Fe}_2\text{O}_3$  ratio of 1:4).

To estimate the  $q_{\text{TI}}$  due to devolatilization fluids exiting the top of the slab, we took  $38,500 \text{ km}$  as the effective trench length<sup>21,24</sup>, a convergence rate of  $6.2 \text{ cm yr}^{-1}$  (refs. <sup>21,24</sup>), a  $45^\circ$  slab dip angle and a fluid density of  $1,150 \text{ kg m}^{-3}$ . This density represents the range for  $\text{H}_2\text{O}$  from  $1,090 \text{ kg m}^{-3}$  at  $500^\circ\text{C}$  and  $1.5 \text{ GPa}$  to  $1,210 \text{ kg m}^{-3}$  at  $700^\circ\text{C}$  and  $3.0 \text{ GPa}$  (ref. <sup>66</sup>). With these values, we calculated  $q_{\text{TI}}$  in the range  $210 \text{ m}^3 \text{ m}^{-2}$  (ref. <sup>24</sup>) to  $230 \text{ m}^3 \text{ m}^{-2}$  (ref. <sup>21</sup>) for the  $80$ – $150 \text{ km}$  depth interval; we used  $220 \text{ m}^3 \text{ m}^{-2}$  herein. Note that this value included metasedimentary devolatilization; however,  $94\%$  of the flux is generated by underlying altered oceanic crust and serpentinite<sup>21,24</sup>. Subtracting the metasedimentary contribution yielded  $\sim 200$ – $220 \text{ m}^3 \text{ m}^{-2}$ , which is within the uncertainties of the calculation.

With the values of  $M_s$ ,  $\Delta X_s$ ,  $V_f$  and  $\phi$  in hand, we could solve equation (5) for  $L$ , given the  $q_{\text{TI}}$  value. So, for the O–H fluid example, assuming reduction of  $2.5 \text{ wt}\%$   $\text{Fe}_2\text{O}_3$ , we have  $M_{\text{H}_2} = 2.5 \times 2.004 \times 10^2 \text{ moles H}_2 \text{ m}^{-3}_{\text{rock}}$ ;  $\Delta X_{\text{H}_2} = 6.094 \times 10^{-5}$ ;  $V_f = 1.495 \times 10^{-5} \text{ m}^3 \text{ mol}^{-1}$ ;  $\phi = 0.001$ ; and  $q_{\text{TI}} = 220 \text{ m}^3 \text{ m}^{-2}$ . Solving equation (5) for  $L$  yielded  $L = 1.8 \text{ m}$ . Consequently, a metasedimentary layer  $\sim 2 \text{ m}$  thick that has  $2.5 \text{ wt}\%$   $\text{Fe}_2\text{O}_3$  available for reduction will oxidize (remove the  $\text{H}_2$  from) the entire slab dehydration flux of  $220 \text{ m}^3 \text{ m}^{-2}$ .

The thickness of metasediment required for  $\text{H}_2$  oxidation is remarkably small, but  $\text{CH}_4$  and  $\text{H}_2\text{S}$  oxidation will involve greater thicknesses. Considerable amounts of sediment cover slabs worldwide<sup>81</sup>; we took the average thickness of the metasedimentary sequence to be  $400 \text{ m}$  (ref. <sup>24</sup>). This is probably a minimum average, because vertical fluid flow up through such a sequence dipping at  $45^\circ$  along the slab would actually traverse a distance of  $\sim 570 \text{ m}$ . Steeper dips would lead to even greater thicknesses. This would provide appreciably more oxidizing power than the  $400 \text{ m}$  we consider; thus, our conclusions are conservative.

The largest subarc time-integrated fluid flux estimates of which we are aware are  $\sim 300 \text{ m}^3 \text{ m}^{-2}$  (ref. <sup>82</sup>). These would increase the length scales of flow needed for metasedimentary fluid oxidation, but all examples in Fig. 4b would remain  $<275 \text{ m}$ . For example, for representative  $5 \text{ wt}\%$   $\text{Fe}_2\text{O}_3$  reduction via an S–O–H fluid (DEW model), the redox front  $L$  is still only  $\sim 130 \text{ m}$ , much smaller than typical metasediment thicknesses.

If diffusion and mechanical dispersion operated in addition to advection and/or if there were kinetic departures from local fluid–rock equilibrium, redox fronts would be smeared out to some degree but the  $L$  is still valid for  $q_{\text{TI}}$  estimation<sup>37–39</sup>. Diffusive mass transfer will occur adjacent to conduits such as veins (Fig. 2e). These features are too small to resolve individually with our methods but are incorporated in a general way by the continuum approach of equation (4). Fluid channelization at larger scales in subduction complexes is well documented<sup>80</sup>, for example in metaigneous rocks below the metasedimentary cover<sup>21,51</sup>, in veins<sup>21,83</sup> and along lithologic contacts<sup>52,83,84</sup>, but reaction progress and oxygen isotope evidence indicate that fluxes within the metasedimentary units of the CBU were largely pervasive<sup>13</sup>.

It is difficult for oxidized fluids to change the redox state of rocks that are already highly oxidized<sup>39,40</sup> (that is, very large fluid fluxes would be needed). Thus, it is not uncommon to find highly oxidized intercalated rock layers with differing  $f_{\text{O}_2}$  values<sup>32</sup>. However, if such sequences were infiltrated by fluids with substantially lower  $f_{\text{O}_2}$ , reduction would occur as described herein and in refs. <sup>39,40</sup>.

**Rock descriptions.** White mica refers to undifferentiated K-rich and/or Na-rich micas. The samples are listed in the approximate order of decreasing  $f_{\text{O}_2}$ . Extended Data Fig. 1 shows the sample locations and general geologic relations for Tinos<sup>43,85,86</sup>.

1. Sample jagan1A. Mn- and Fe-rich quartzitic schist, Andros (Fig. 1b). Composed mainly of quartz, Mn-bearing epidote and garnet, white mica, chlorite and haematite. The epidote can contain an appreciable piemontite ( $\text{Ca}_2\text{Mn}^{2+}\text{Al}_2\text{Si}_3\text{O}_{12}(\text{OH})$ ) component. The most Mn-rich compositions occur in the cores of grains that form aggregates several millimetres in diameter (Fig. 1b). We speculate that these were originally small seafloor Mn nodules. Epidote rims in contact with matrix minerals have considerably less Mn; these were used for  $f_{\text{O}_2}$  estimation. Garnets are rich in the spessartine component ( $\text{Mn}_3\text{Al}_2\text{Si}_3\text{O}_{12}$ ). Location:  $37^\circ 53.587' \text{ N}$ ,  $24^\circ 55.172' \text{ E}$ .
2. Sample jagcr00A. Phyllite cut by  $3.5\text{-cm}$ -wide metamorphic quartz vein, Crete (Fig. 2e). The outcrop is highly veined; carpholite is common in veins cutting rocks of appropriate bulk composition. Rock distal to the vein is a purplish-red phyllite that consists predominantly of phengite, paragonite, quartz, haematite and rutile. The altered selvage rock adjacent to the vein has a bleached appearance due to the nearly complete destruction of haematite. The vein contains siderite–magnesite ( $\text{FeCO}_3$ – $\text{MgCO}_3$ ) solid solution. This suggests a reaction in which  $\text{CH}_4$  reacted with  $\text{Fe}_2\text{O}_3$  to produce  $\text{FeCO}_3$ . We quantify the  $f_{\text{O}_2}$  for the haematite-bearing phyllite using the HIR reaction. Further work is needed to quantify the  $f_{\text{O}_2}$  in the

- vein and selvage, but the destruction of haematite and the production of carbonate indicate a metamorphic  $f_{O_2}$  decrease. Location: Kerames village area, 35°09.805' N, 24°30.777' E
3. Sample 57-29. Metabauxite from Naxos described by Feenstra<sup>35</sup> containing diaspore and haematite together with rutile, calcite, white mica and margarite. This rock is from the low-grade regional zone I and thus was not strongly overprinted by the later Barrovian metamorphism that affected other parts of the island. Location: 35°57.667' N, 25°33.083' E. A comparable rock from Crete (sample jagcr10A) is shown in Fig. 1a; its location is: 35°23.153' N, 24°53.672' E.
  4. Sample jagti86F. Micaceous schist, Tinos, which contains white mica, Na amphibole, epidote, quartz, calcite (inferred former aragonite), dolomite–ankerite solid solution, sphene and haematite. The assemblage haematite + sphene + calcite is widespread in the metasediments of Tinos. Given constraints on the activity of  $CO_2$  in the fluid<sup>43</sup>, the  $f_{O_2}$  can be estimated for such rocks via equilibrium IHAS. Location: 37°35.834' N, 25°04.664' E.
  5. Sample jagti108C. Micaceous schist, Tinos (Fig. 1e). This is representative of a very common rock type on Tinos, composed predominantly of phengite + epidote + quartz + chlorite + haematite + rutile or sphene ± albite ± carbonates ± Na-bearing amphibole/clinopyroxene. The high-pressure/low-temperature origin of such rocks is clear, as phengite is very Si rich and can attain 3.52 Si per formula unit (see Data availability). Veins and adjacent selvages in such rocks can contain coarse haematite and rutile (Fig. 1f). Location: 37°32.693' N, 25°13.634' E.
  6. Sample jagti134N. Magnetite + haematite + garnet quartzite, Tinos (Fig. 2a). Garnet cores contain only haematite inclusions, whereas the matrix contains magnetite and haematite. Matrix magnetite grew around garnet with haematite inclusions, demonstrating a decrease in  $f_{O_2}$  associated with reduction (Fig. 3). Location: 37°33.221' N, 25°12.742' E.
  7. Sample jagti90B. Quartzite, Tinos, that contains substantial Na amphibole and Mn-rich garnet (Fig. 1c). Garnet has inclusions of haematite-rich rhombohedral oxide whereas the matrix contains Mn-bearing ilmenite that grew around garnet (Fig. 2d). These textures document a metamorphic decrease in  $f_{O_2}$  (Fig. 3). Location: 37°37.454' N, 25°02.833' E.
  8. Sample jagti68B. Marble composed mostly of calcite (inferred former aragonite), glaucophane–riebeckite Na amphibole, Na–Ca amphibole, magnetite and haematite, together with minor chlorite, epidote and quartz. Tinos (Fig. 1d). Location: 37°33.697' N, 25°13.405' E.
  9. Sample jagti75A. Albitite schist, Tinos. A complex rock consisting of albite, quartz, phengite, magnetite, haematite, epidote, Na and Na–Ca amphiboles, and sphene. Rare  $Fe^{3+}$ -bearing sodic clinopyroxene (jadeite–aegirine) can be found as inclusions in Na amphibole and in the matrix. The rock is cut by anastomosing veinlets in which haematite has been converted to magnetite (Fig. 2b). We interpret these anastomosing features to be the fossil flow paths of infiltrating reducing fluids that reduced haematite to magnetite. The  $f_{O_2}$  must have been near haematite–magnetite values during this process. Location: 37°35.764' N, 25°04.483' E.
  10. Sample jagti106B. Schist, Tinos. A garnetiferous schist rich in epidote which also contains phengite, chlorite, albite and magnetite. The garnets include haematite, rutile, magnetite, Na amphibole and probable lawsonite pseudomorphs. Cooling-related exsolution lamellae are present in haematite. Sodium amphibole in the matrix is largely or completely replaced by aggregates of chlorite and albite. The rock contains appreciable dark bluish-green tourmaline throughout. Location: 37°32.821' N, 25°13.643' E.
  11. Sample jagti154F. Micaceous Na amphibole schist, Tinos, characterized by Na amphibole, phengite, epidote and porphyroblasts of garnet. Rutile and rhombohedral oxides are found as inclusions in garnet, whereas the matrix, garnet rims and Na amphibole contain sphene. Garnets have inclusions of  $Fe^{3+}$ -bearing Na–Ca amphibole in their interiors which have a ~25% greater  $Fe^{3+}/(Fe^{2+} + Fe^{3+})$  ratio than matrix Na amphibole (Fig. 2c). Garnet also contains inclusions of clinopyroxene dominated by jadeite–aegirine with ~0.4–0.6  $Fe^{3+}/(Fe^{3+} + Al)$ , as well as epidote. Magnetite (now martite) is found in the matrix and in contact with garnet rims. The rhombohedral oxides contain complex exsolution lamellae and replacement textures; we infer that two rhombohedral oxides coexisted during high-pressure/low-temperature metamorphism. Location: 37°33.358' N, 25°06.430' E.
  12. Sample jagti90A. Metabasaltic blueschist dominated by Na amphibole, epidote and garnet, with lesser amounts of quartz, rhombohedral oxides, rutile and magnetite. Titanium-bearing haematite and  $Fe^{3+}$ -bearing ilmenite are present, both of which contain exsolution lamellae. This indicates crystallization on the haematite–ilmenite solvus, followed by exsolution during cooling. The sample is intercalated with oxidized metasediments (for example, sample jagti90B) raising the possibility that metabasalts become oxidized due to redox exchange with metasediments, in addition to other processes such as seafloor hydrothermal alteration. Location: 37°37.454' N, 25°02.833' E.
  13. Sample jagti93E. Micaceous phengite, Na amphibole, garnet, quartz, chloritoid schist that contains finely disseminated graphitic carbon. Rutile and ilmenite coexist in garnet cores, transitioning to sphene in garnet rims and the matrix. The  $f_{O_2}$  estimate is for the core assemblage of rutile + ilmenite. Location: 37°37.375' N, 25°02.850' E.

## Data availability

The electron-probe microanalyses of minerals can be downloaded from <https://doi.org/10.5281/zenodo.5809204>. The rock samples and petrographic thin sections are in the collections of the Yale Peabody Museum of Natural History, Division of Mineralogy and Meteoritics.

## Code availability

The THERMOCALC<sup>65</sup> (version 3.37) program can be accessed at <https://hpxeosandthermocalc.org/> and the AX 62 program can be accessed at <https://filedn.com/U1UGlyFhv3UuXg5E9dbnWFF/TJBHpages/ax.html>. The Theriak-Domino software<sup>72</sup> is available at <https://titan.minpet.unibas.ch/minpet/theriak/theruser.html>.

## References

57. Whitney, D. L. & Evans, B. W. Abbreviations for names of rock-forming minerals. *Am. Mineral.* **95**, 185–187 (2010).
58. Hawthorne, F. C. et al. Nomenclature of the amphibole supergroup. *Am. Mineral.* **97**, 2031–2048 (2012).
59. Trotet, F., Jolivet, L. & Vidal, O. Tectono-metamorphic evolution of Syros and Sifnos islands (Cyclades, Greece). *Tectonophysics* **338**, 179–206 (2001).
60. Behr, W. M., Kotowski, A. J. & Ashley, K. T. Dehydration-induced rheological heterogeneity and the deep tremor source in warm subduction zones. *Geology* **46**, 475–478 (2018).
61. Skelton, A. et al. Preservation of high-P rocks coupled to rock composition and the absence of metamorphic fluids. *J. Metamorph. Geol.* **37**, 359–381 (2019).
62. Fassoulas, C. G., Rahl, J. M., Ague, J. J. & Henderson, K. Patterns and conditions of deformation in the Plattenkalk nappe, Crete, Greece: a preliminary study. *Bull. Geol. Soc. Greece XXXVI*, 1626–1635 (2004).
63. Stöckhert, B., Wachmann, M. & Schwarz, S. Structural evolution and rheology of high-pressure–low-temperature metamorphic rocks. *Boch. Geolog. Geotechn. Arb.* **44**, 235–242 (1995).
64. Thomson, S. J., Stöckhert, B. & Brix, M. R. Thermochronology of the high-pressure metamorphic rocks of Crete, Greece: implications for the speed of tectonic processes. *Geology* **26**, 259–262 (1998).
65. Holland, T. J. B. & Powell, R. An improved and extended internally consistent thermodynamic dataset for phases of petrological interest, involving a new equation of state for solids. *J. Metamorph. Geol.* **29**, 333–383 (2011).
66. Pitzer, K. S. & Sterner, S. M. Equations of state valid continuously from zero to extreme pressures for  $H_2O$  and  $CO_2$ . *J. Chem. Phys.* **101**, 3111–3116 (1994).
67. Holland, T. & Powell, R. A Compensated-Redlich-Kwong (CORK) equation for volumes and fugacities of  $CO_2$  and  $H_2O$  in the range 1 bar to 50 kbar and 100–1600 °C. *Contrib. Mineral. Petrol.* **109**, 265–273 (1991).
68. Holland, T. J. B. & Powell, R. Activity–composition relations for phases in petrological calculations: an asymmetric multicomponent formulation. *Contrib. Mineral. Petrol.* **145**, 492–501 (2003).
69. Evans, K. A. & Powell, R. The effect of subduction on the sulfur, carbon, and redox budget of lithospheric mantle. *J. Metamorph. Geol.* **33**, 649–670 (2015).
70. Shi, P. & Saxena, S. K. Thermodynamic modeling of the C–H–O–S fluid system. *Am. Mineral.* **77**, 1038–1049 (1992).
71. Mel'nik, Y. P. *Thermodynamic Properties of Gases under Conditions of Deep Petrogenesis* (Naukova Dumka, 1978).
72. de Capitani, C. & Petrakakis, K. The computation of equilibrium assemblage diagrams with Theriak/Domino software. *Am. Mineral.* **95**, 1006–1016 (2010).
73. White, R. W., Powell, R., Holland, T. J. B., Johnson, T. E. & Green, E. C. R. New mineral activity–composition relations for thermodynamic calculations in metapelitic systems. *J. Metamorph. Geol.* **32**, 261–286 (2014).
74. White, R. W., Powell, R. & Johnson, T. E. The effect of Mn on mineral stability in metapelites revisited: new  $a-x$  relations for manganese-bearing minerals. *J. Metamorph. Geol.* **32**, 809–828 (2014).
75. Green, E. C. R. et al. Activity–composition relations for the calculation of partial melting equilibria in metabasic rocks. *J. Metamorph. Geol.* **34**, 845–869 (2016).
76. Ague, J. J., Baxter, E. F. & Eckert, J. O. Jr. High  $f_{O_2}$  during sillimanite zone metamorphism of part of the Barrovian type locality, Scotland. *J. Petrol.* **42**, 1301–1320 (2001).
77. Donohue, C. L. & Essene, E. J. An oxygen barometer with the assemblage garnet–epidote. *Earth Planet. Sci. Lett.* **181**, 459–472 (2000).
78. Ague, J. J. & Brimhall, G. H. Regional variations in bulk chemistry, mineralogy, and the compositions of mafic and accessory minerals in the batholiths of California. *Geol. Soc. Am. Bull.* **100**, 891–911 (1988).
79. Philpotts, A. R. & Ague, J. J. *Principles of Igneous and Metamorphic Petrology* 2nd edn (Cambridge Univ. Press, 2009).



80. Taetz, S., John, T., Bröcker, M., Spandler, C. & Stracke, A. Fast intraslab fluid-flow events linked to pulses of high pore fluid pressure at the subducted plate interface. *Earth Planet. Sci. Lett.* **482**, 33–43 (2018).
81. Plank, T. & Langmuir, C. H. The chemical composition of subducting sediment and its consequences for the crust and mantle. *Chem. Geol.* **145**, 325–394 (1998).
82. Zack, T. & John, T. An evaluation of reactive fluid flow and trace element mobility in subducting slabs. *Chem. Geol.* **239**, 199–216 (2007).
83. Ague, J. J. & Nicolescu, S. Carbon dioxide released from subduction zones by fluid-mediated reactions. *Nat. Geosci.* **7**, 355–360 (2014).
84. Breeding, C. M., Ague, J. J. & Bröcker, M. Fluid-metasedimentary rock interactions and the chemical composition of arc magmas. *Geology* **32**, 1041–1044 (2004).
85. Melidonis, N. G. The geological structure and mineral deposits of Tinos Island (Cyclades, Greece). *Geol. Greece* **13**, 1–80 (1980).
86. Bröcker, M. & Franz, L. Rb–Sr isotope studies on Tinos Island (Cyclades, Greece): additional time constraints for metamorphism, extent of infiltration-controlled overprinting and deformational activity. *Geol. Mag.* **135**, 369–382 (1998).

## Acknowledgements

We thank C. M. Breeding, M. Bröcker, E. L. Donald, D. S. Keller, D. Levy, S. A. Menemenlis, E. M. Stewart, M. Tian and D. E. Wilbur for discussions and fieldwork, and J. O. Eckert Jr for assistance with electron-probe microanalysis. We gratefully acknowledge funding provided by the US National Science Foundation Directorate of Geosciences (grant numbers EAR-0105927, EAR-0744154 and EAR-1650329 to J.J.A.; grant number EAR-1855208 to M.E.H.), Yale University and the Yale Peabody Museum of Natural History (J.J.A.), a Bateman Postdoctoral Fellowship, Department of Earth and Planetary Sciences, Yale University (S.T.), the National Natural Science Foundation of China (grant number 42122011 to J.-L.L.) and the Deutsche Forschungsgemeinschaft (DFG) through grant number CRC 1114

'Scaling Cascades in Complex Systems', Project Number 235221301, Project (C09) – 'Dynamics of Rock Dehydration on Multiple Scales' (T.J.).

## Author contributions

J.J.A. designed the study, coordinated the fieldwork and collected samples, performed the electron probe microanalysis, prepared the petrographic thin sections and did the pseudosection and time-integrated fluid flux calculations. S.T., M.E.H., E.C. and J.-L.L. provided perspectives and conceptual advice and guidance on model development and the oxygen fugacity of arc lavas in relation to subducted oceanic lithosphere. J.J.A., J.-L.L. and M.E.H. performed oxygen fugacity calculations and uncertainty analysis. J.-L.L., E.M.S., T.J., S.T. and J.J.A. constrained the sulfur mass balance, and C.F. provided guidance in the field, including the location of key outcrops. All authors contributed extensively to the interpretation of the data, discussions and preparation of the manuscript.

## Competing interests

The authors declare no competing interests.

## Additional information

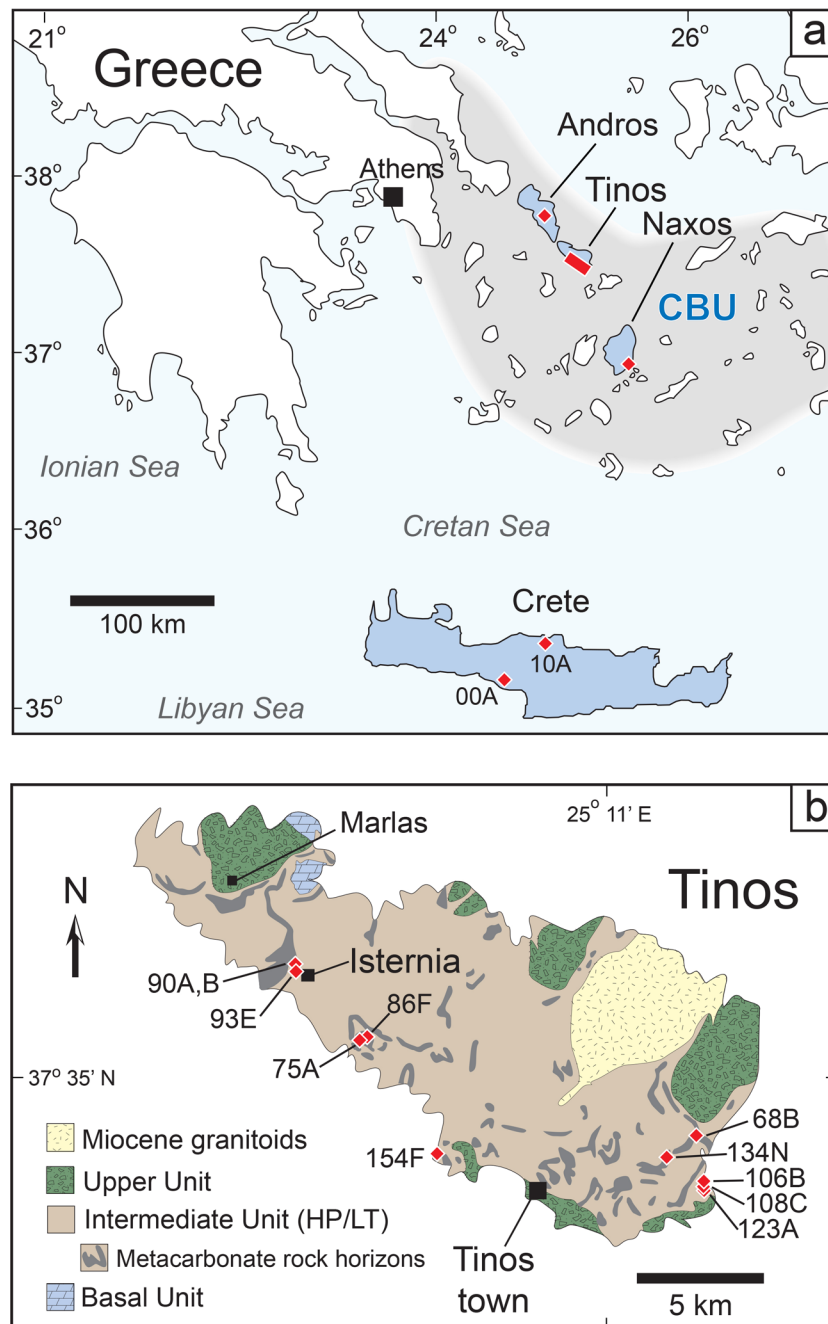
**Extended data** is available for this paper at <https://doi.org/10.1038/s41561-022-00904-7>.

**Supplementary information** The online version contains supplementary material available at <https://doi.org/10.1038/s41561-022-00904-7>.

**Correspondence and requests for materials** should be addressed to Jay J. Ague.

**Peer review information** *Nature Geoscience* thanks Dimitri Sverjensky and Sarah Penniston-Dorland for their contribution to the peer review of this work. Primary Handling Editor: Rebecca Neely, in collaboration with the *Nature Geoscience* team.

**Reprints and permissions information** is available at [www.nature.com/reprints](http://www.nature.com/reprints).



**Extended Data Fig. 1 | Location maps.** Location maps. a, Aegean region showing Crete and the extent of the Cycladic high-pressure/low-temperature (HP/LT) metamorphic belt (Cycladic Blueschist Unit; CBU). Sample locations are shown with red symbols. b, Generalized geologic map of Tinos showing sample locations. Map adapted from ref. <sup>43</sup>, Springer Nature Limited; field relations from refs. <sup>43,85,86</sup>.